Monthly Notices
of the
ROYAL ASTRONOMICAL SOCIETY

MNRAS **470,** 4133–4144 (2017)
Advance Access publication 2017 June 7

doi:10.1093/mnras/stx1383

A deeper look at the X-ray point source population of NGC 4472

T. D. Joseph,[1,2,4★] T. J. Maccarone,[3,2] R. P. Kraft[4] and G. R. Sivakoff[5]

[1] *University of Cape Town, Rondebosch 7701, Republic of South Africa*
[2] *University of Southampton, Southampton SO17 1BJ, UK*
[3] *Texas Tech University, Lubbock, TX 79409-1051, USA*
[4] *Harvard/Smithsonian Center for Astrophysics, 60 Garden Street, MS-4, Cambridge, MA 02138, USA*
[5] *University of Alberta, Edmonton Alberta T6G 2E1, Canada*

Accepted 2017 June 2. Received 2017 June 1; in original form 2017 January 17

ABSTRACT

In this paper we discuss the X-ray point source population of NGC 4472, an elliptical galaxy in the Virgo cluster. We used recent deep *Chandra* data combined with archival *Chandra* data to obtain a 380 ks exposure time. We find 238 X-ray point sources within 3.7 arcmin of the galaxy centre, with a completeness flux, $F_{\mathrm{X,\,0.5\text{-}2\,keV}} = 6.3 \times 10^{-16}$ erg s^{-1} cm^{-2}. Most of these sources are expected to be low-mass X-ray binaries. We finding that, using data from a single galaxy which is both complete and has a large number of objects (∼100) below 10^{38} erg s^{-1}, the X-ray luminosity function is well fitted with a single power-law model. By cross matching our X-ray data with both space based and ground based optical data for NGC 4472, we find that 80 of the 238 sources are in globular clusters. We compare the red and blue globular cluster subpopulations and find red clusters are nearly six times more likely to host an X-ray source than blue clusters. We show that there is evidence that these two subpopulations have significantly different X-ray luminosity distributions. Source catalogues for all X-ray point sources, as well as any corresponding optical data for globular cluster sources, are also presented here.

Key words: stars: low mass – X-rays: binaries – X-rays: individual: NGC 4472.

1 INTRODUCTION

The *Chandra X-ray Observatory* (Weisskopf et al. 2000) has made it possible to carry out detailed studies of low-mass X-ray binaries (LMXBs) beyond the Local Group, allowing us to probe these systems in a wide variety of galactic environments. LMXBs can be formed either at the end point of stellar evolution. These binaries can also be produced in globular clusters (GCs) via *N*-body capture (Clark 1975; Fabian, Pringle & Rees 1975; Hills 1976) or direct collisions between compact objects and red giant stars (Verbunt 1987). Yet, despite all we know about them, many unanswered questions about LMXBs still remain. Is the LMXB X-ray luminosity function universal across all galaxies? Is there a difference between LMXBs found in the field of the galaxy and those found in GCs? Why do these X-ray sources prefer red GCs over blue ones? The GC-LMXB relationship is of particular interest as these clusters appear to be a rich environment for LMXBs. It is necessary to study nearby elliptical galaxies and their GC systems to gain a better understanding of the issues related to LMXB formation and evolution.

NGC 4472 is a massive (8×10^{11} M$_{\odot}$; Côté et al. 2003), nearby elliptical galaxy that is falling into the Virgo cluster ($d = 16$ Mpc; e.g. Macri et al. 1999). It contains much less bright diffuse X-ray gas than other massive nearby ellipticals such as M 87 and NGC 1399, making it easier to probe fainter X-ray point sources within the galaxy. NGC 4472 has a system of roughly 6000 globular clusters (Rhode & Zepf 2001) and is therefore an excellent environment in which to study the GC-LMXB connection.

Kundu, Maccarone & Zepf (2002) studied the X-ray point source population of NGC 4472 using a 40 ks *Chandra* observation and archival *Hubble Space Telescope* (*HST*) data (see also Kundu & Whitmore 2001). They considered only X-ray data from the *Chandra* ACIS–S3 chip and excluded the central 8 arcsec due to the high background in this region. A total of 144 X-ray sources were detected. This study found that the spatial distribution of the GCs, the GC-LMXBs and the field LMXBs were similar. They showed that 30 of the 72 LMXBs situated within the *HST* fields were coincident with GCs. The subsequent work of Maccarone, Kundu & Zepf (2003, hereafter MKZ03) found no statistically significant differences between the X-ray properties of the GC and field LMXBs. These findings could imply that a significant proportion of field LMXBs were created in GCs and then ejected from the cluster due to dynamical interactions or the destruction of the cluster.

★ E-mail: tana@saao.ac.za

Table 1. A list of all the *Chandra* observations of NGC 4472 used in this work.

Date	Obs ID	Exposure time (ks)
2000 June 12	321	40
2010 February 27	11 274	40
2011 February 14	12 889	140
2011 February 21	12 888	160

More recent deep *Chandra* data has become available for NGC 4472. By combining these data with archival observations we should be able to detect enough X-ray sources to carry out robust comparisons of various LMXB populations within the galaxy.

2 OBSERVATIONS AND DATA ANALYSIS

In this work we used both archival and recent *Chandra* observations of NGC 4472 to study its X-ray point source population. All the data were taken with ACIS-S. The most recent data were taken in 2011 on February 14 (Obs ID 12889) and February 21 (Obs ID 12888); with exposure times of 140 ks and 160 ks, respectively. Two shorter observations of 40 ks each were also used, giving a total exposure time of 380 ks. The more recent of the two (Obs ID 11274; Maccarone et al. 2010) was taken on 2010 February 27 and the oldest observation (Obs ID 321; Kundu et al. 2002) was taken on 2000 June 12. These data are summarized in Table 1.

All the data sets were first reprocessed with the CIAO[1] script *chandra_repro* using calibration data from 2011 March. New level two event files were created for all the observations using this script. The data were then checked for background flares and these were eliminated. The event files and images were restricted to the well calibrated 0.5–5 keV range using the CIAO command *dmcopy*.

Exposure maps were created for each CCD chip of each observation using the *asphist*, *mkinstmap* and *mkexpmap* scripts. Point spread function (PSF) files were produced using *mkpsfmap* to determine the size of the PSF at each position on the images. The exposure maps and PSF file data were then used by the point source detection script *wavdetect* with a false source detection probability threshold of 10^{-7} to correctly identify point sources in the images.

All sources within 8 arcsec of the galaxy centre were excluded to avoid the area of very high X-ray background, consistent with the work of Kundu et al. (2002). Furthermore, only sources within 3.7 arcmin of the galaxy centre were included in this study, to avoid areas close to the CCD edges that were not adjacent to another CCD and to exclude the regions with substantially enlarged PSF. Thus we only include sources from ACIS-S3 and ACIS-S4 in this work.

We obtained a counts-to-energy conversion factor by comparing the fluxes of two bright sources with their respective net count rate. The spectrum of a bright source that had a disc blackbody (diskbb) continuum with an inner disc temperature, $kT = 1.5$ keV, and one that had a power-law (PL) continuum with $\Gamma = 1.7$ were analysed in ISIS and fluxes and flux errors were obtained. The respective net count rates (net counts per source divided by the net exposure) and the corresponding errors were obtained from *wavdetect*. The counts-to-energy conversion factor was then calculated by dividing the flux obtained through spectral fitting by the net count rate of each source. These conversion factors were then used to calculate the X-ray fluxes for both diskbb and PL models for the rest of the X-ray point sources using their respective count rates. The errors

[1] http://cxc.harvard.edu/ciao4.4/threads/index.html

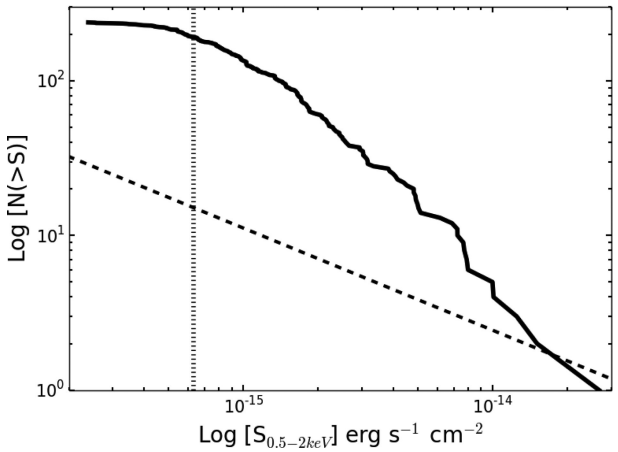

Figure 1. The log N–log S plot for the entire X-ray point source sample. The dotted vertical line indicates the 0.5–2 keV completeness limit and the dashed line indicates the number of background sources as a function of flux (see equation 1 in Tozzi et al. 2001).

for the flux values were calculated by using the flux errors obtained from ISIS for the two bright sources mentioned above and the errors on the count rate obtained from *wavdetect* and propagating them in the standard way.

A 4 σ completeness limit was calculated for the combined 380 ks data set. Using the smoothed background image of the data set created in *wavdetect*, the number of background counts at each source position was determined using the region enclosing 90 per cent of the source energy. This gives the background sensitivity as a function of position. The 4 σ upper limit was then calculated and these background counts were then converted to flux values using the counts-to-energy conversion factor. It was found that the diffuse X-ray emission in the central region of the galaxy dominated the background sensitivity and the completeness limit was determined based on the flux values in that region.

We made use of the TOPCAT programme (Taylor 2005) to search for sources coincident with GCs found in both ground (Rhode & Zepf 2001) and space based (Jordán et al. 2009) optical observations. Rhode & Zepf (2001, hereafter RZ01) surveyed the GC system of NGC 4472 using *B, V* and *R* filters. The survey field covers the central 0.66–23 arcmin region of the galaxy and 1465 GCs were detected.

Jordán et al. (2009) surveyed the GC system of the inner region of NGC 4472 using the F475W and F850LP bandpasses as part of their Virgo Cluster Survey (VCS). These bandpasses are approximately equivalent to the Sloan *g* and *z* filters, respectively and will be referred to as such in the rest of this work. The VCS covers the central 3.3× 3.3 arcmin of the galaxy (see Côté et al. 2004); 764 GCs were detected in this region of NGC 4472.

MKZ03, using Obs ID 321, found 30 X-ray sources coincident with GCs. They used archival *HST* observations that covered central region as well as the halo of NGC 4472 (see Fig. 1 in Kundu et al. 2002) and used *V* and *I* filters (see Kundu & Whitmore 2001). We cross matched the GC source list of MKZ03 with our source catalogue using the *Chandra* coordinates to try to identify more GC X-ray sources.

We estimated the boresight corrections for the X-ray positions by calculating the weighted mean offset between obvious initial matches of the optical and X-ray data. The RZ01 data had offsets of −0.25 arcsec(RA) and −0.50 arcsec (Dec.), while the VCS positions had offsets of 0.18 arcsec and 0.10 arcsec for RA and Dec.,

Table 2. A sample of the table of X-ray fluxes of the sources within 3.7 arcmin of the galaxy centre. The fluxes are in units of erg s^{-1} cm^{-2}. The PL and DBB subscripts denote the spectral model conversion factor used to calculate the flux. The 'err' designation denotes flux errors. The flag column identifies sources that are interesting and/or for which caution must be used when analysing the source properties. The key is as follows: bkg = source in an area of high background; c = *wavdetect* has misidentified or not detected the source in one of the observations; cg = the source is in or very close to a chip gap in one of the observations; and GC = the source is associated with a globular cluster.

RA (degrees)	Dec. (degrees)	$Flux_{PL}$ (0.5–5 keV)	$Flux_{PL}$ err (0.5–5 keV)	$Flux_{PL}$ (0.5–2 keV)	$Flux_{PL}$ err (0.5–2 keV)	$Flux_{DBB}$ (0.5–5 keV)	$Flux_{DBB}$ err (0.5–5 keV)	$Flux_{DBB}$ (0.5–2 keV)	$Flux_{DBB}$ err (0.5-2 keV)	Flag
187.499 77	8.020 63	1.456E-14	1.724E-15	7.641E-15	9.052E-16	1.536E-14	1.829E-15	6.248E-15	7.436E-16	–
187.498 04	8.029 89	9.137E-16	2.96E-16	4.795E-16	1.553E-16	9.639E-16	3.125E-16	3.921E-16	1.271E-16	–
187.497 57	7.998 43	1.097E-15	2.586E-16	5.759E-16	1.357E-16	1.158E-15	2.732E-16	4.709E-16	1.111E-16	–
187.491 75	7.967 68	2.955E-15	7.334E-16	1.551E-15	3.849E-16	3.118E-15	7.746E-16	1.268E-15	3.151E-16	–
187.4915	7.968 26	1.831E-15	3.881E-16	9.61E-16	2.037E-16	1.932E-15	4.101E-16	7.858E-16	1.668E-16	–
187.490 98	7.991 21	1.57E-15	3.028E-16	8.242E-16	1.589E-16	1.657E-15	3.201E-16	6.739E-16	1.302E-16	–
187.490 21	7.9924	1.708E-15	3.068E-16	8.962E-16	1.611E-16	1.801E-15	3.245E-16	7.328E-16	1.32E-16	GC

respectively. These mean offsets were then applied to the X-ray positions.

We experimented with several different matching radii for the RZ01 and VCS catalogues. For the VCS catalogue, it was found that a matching radius of 0.5 arcsec produced only 36 matches between X-ray and optical sources whereas a 0.75 arcsec matching radius produced nearly twice as many. A 1 arcsec matching radius yielded as many matches as the 0.75 arcsec matching radius and thus we adopted the latter in our work.

For the RZ01 catalogue, we tried various matching radii in the range 0.75–2 arcsec. We found that a matching radius of 1.25 arcsec provided a good number of matches without being so large as to include non-coincident sources.

The false match probability for matches between the optical and X-ray data were determined by shifting each X-ray source position by a distance much greater than the matching radius and much smaller than the field of view and then seeing how many matches were found. In this case, the shift value used was 10 arcsec.

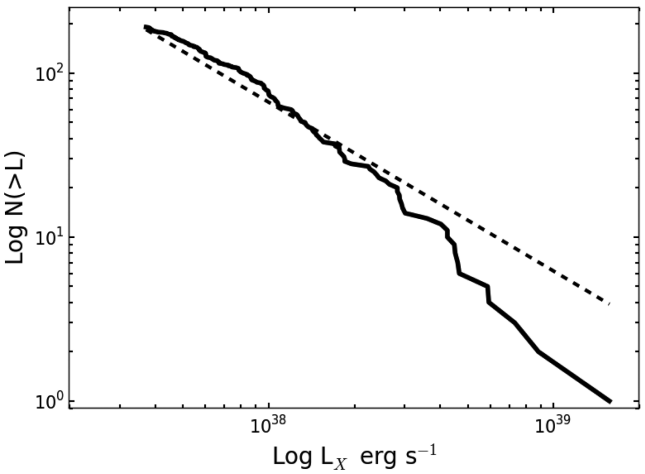

Figure 2. The X-ray luminosity function for the completeness limited X-ray point source sample (solid line) with the best-fitting function over plotted (dotted line). The luminosity is for the 0.5–5 keV range.

3 RESULTS AND DISCUSSION

3.1 X-ray point source population

We find 238 sources within 3.7 arcmin of the galactic centre, 70 of which are bright enough to be detected in all four observations. 191 sources are found to be brighter than 6.3×10^{-16} erg s^{-1} cm^{-2} (0.5–2 keV; $L_{X,\,0.5\text{-}5\,keV} = 3.7 \times 10^{37}$ erg s^{-1}), the 4 σ completeness limit for the combined data set. We expect roughly 10 of the X-ray sources to be background active galactic nucleus (AGN) at this completeness limit (Tozzi et al. 2001). Data for AGN counts are generally given for a soft band (0.5–2 keV) and a harder band. Since it was not possible to find AGN X-ray luminosity function (XLF) data present specifically for the 0.5–5 keV band we use in the rest of the paper, we present the 0.5–2 keV data for the AGN data as well as our own X-ray point source data for NGC 4472. We also note that the soft band AGN slope is shallower than the hard band slope estimates, thus using the 0.5–2 keV AGN data provides a slight overestimate of the number of expected background AGNs. These data are summarized in Fig. 1.

A list of the X-ray luminosities of the sources can be found in Table 3. A sample of this table is shown in Table 2.

We have constructed the XLF for NGC 4472 using multi-epoch data. One might therefore believe that the population of transient X-ray sources in the galaxy would lead to an incorrect XLF. However, Grimm-J., Gilfanov & Sunyaev (2003) point out that XLFs created from *Chandra* observations of the same galaxy taken at different times and even from different parts of the galaxy were not significantly different from each other. Thus we expect that combining observations of NGC 4472 taken at different time, but covering the same area to create one XLF would not lead to an incorrect XLF. Sell et al. (2011) also found that source variability did not change the slope or normalization of an XLF created from merged data sets taken at different epochs compared to XLFs created from individual observations.

We fit a PL function to the differential XLF, using only the completeness limited luminosity data. The function has the form $\frac{dN}{dL_X} = kL_X^{-\beta}$ (see e.g. Gilfanov 2004). To account for the background AGN contamination component, we calculate the expected number of background AGNs using the luminosity function from Tozzi et al. (2001) and subtract this contribution from the observed XLF. We used the XSPEC spectral fitting tool (Arnaud 1996) to fit the PL model to the XLF data, using the Cash statistic.

We find that the best-fitting parameters for the slope and normalization are $\beta = 2.03^{+0.16}_{-0.15}$ and $k = 68.53^{+8.95}_{-8.28}$, respectively. This slope is in good agreement with the results of other studies of the XLF for individual ellipticals as well as the average XLF for an ensemble of elliptical galaxies, where β is typically found to be $\sim$2 (e.g. Gilfanov 2004; Kim & Fabbiano 2004; Kim et al. 2006). The cumulative XLF was constructed by integrating the differential XLF and is shown in Fig. 2.

Table 3. The sources within 3.7 arcmin of the galaxy centre. The fluxes are in units of erg s^{-1} cm^{-2} and the luminosities are in units of erg s^{-1}. The PL and DBB subscripts denote the spectral model conversion factor used to calculate the flux. The 'err' designation denotes flux errors. The flag column identifies sources that are interesting and/or for which caution must be used when analysing the source properties. The key is as follows: bkg = source in an area of high background; c = *wavdetect* has misidentified or not detected the source in one of the observations; cg = the source is in or very close to a chip gap in one of the observations; and GC = the source is associated with a globular cluster.

RA (degrees)	Dec. (degrees)	$Flux_{PL}$ (0.5–5 keV)	$Flux_{PL}$ err (0.5–5 keV)	$Flux_{PL}$ (0.5–2 keV)	$Flux_{PL}$ err (0.5–2 keV)	$Flux_{DBB}$ (0.5–5 keV)	$Flux_{DBB}$ err (0.5–5 keV)	$Flux_{DBB}$ (0.5–2 keV)	$Flux_{DBB}$ err (0.5-2 keV)	Flag
187.499 77	8.020 63	1.46E-14	1.72E-15	7.64E-15	9.05E-16	1.54E-14	1.83E-15	6.25E-15	7.44E-16	–
187.498 04	8.029 89	9.14E-16	2.96E-16	4.8E-16	1.55E-16	9.64E-16	3.13E-16	3.92E-16	1.27E-16	–
187.497 57	7.998 43	1.1E-15	2.59E-16	5.76E-16	1.36E-16	1.16E-15	2.73E-16	4.71E-16	1.11E-16	–
187.491 75	7.967 68	2.96E-15	7.33E-16	1.55E-15	3.85E-16	3.12E-15	7.75E-16	1.27E-15	3.15E-16	–
187.4915	7.968 26	1.83E-15	3.88E-16	9.61E-16	2.04E-16	1.93E-15	4.1E-16	7.86E-16	1.67E-16	–
187.490 98	7.991 21	1.57E-15	3.03E-16	8.24E-16	1.59E-16	1.66E-15	3.2E-16	6.74E-16	1.3E-16	–
187.490 21	7.9924	1.71E-15	3.07E-16	8.96E-16	1.61E-16	1.8E-15	3.25E-16	7.33E-16	1.32E-16	GC
187.4864	7.957 71	1.17E-14	1.4E-15	6.16E-15	7.35E-16	1.24E-14	1.49E-15	5.04E-15	6.04E-16	–
187.485 01	8.002 51	2.7E-15	4.04E-16	1.42E-15	2.12E-16	2.85E-15	4.28E-16	1.16E-15	1.74E-16	–
187.484 83	8.008 48	4.12E-15	5.46E-16	2.16E-15	2.87E-16	4.35E-15	5.78E-16	1.77E-15	2.35E-16	GC
187.484 22	8.013 45	1.04E-15	2.82E-16	5.46E-16	1.48E-16	1.1E-15	2.97E-16	4.46E-16	1.21E-16	–
187.483 01	7.956 25	2.27E-15	4.13E-16	1.19E-15	2.17E-16	2.4E-15	4.37E-16	9.76E-16	1.78E-16	GC
187.482 87	8.000 96	1.57E-15	2.99E-16	8.26E-16	1.57E-16	1.66E-15	3.16E-16	6.75E-16	1.29E-16	GC
187.481 18	8.049 89	1.09E-15	2.85E-16	5.74E-16	1.5E-16	1.15E-15	3.01E-16	4.69E-16	1.23E-16	–
187.476 28	8.016 13	2.62E-15	3.81E-16	1.38E-15	2.0E-16	2.77E-15	4.04E-16	1.13E-15	1.64E-16	–
187.476 02	8.002 71	4.86E-15	6.33E-16	2.55E-15	3.32E-16	5.12E-15	6.71E-16	2.08E-15	2.73E-16	GC
187.475 66	7.955 35	5.98E-15	7.76E-16	3.14E-15	4.08E-16	6.31E-15	8.23E-16	2.57E-15	3.35E-16	–
187.474 88	8.04315	1.48E-15	2.8E-16	7.74E-16	1.47E-16	1.56E-15	2.96E-16	6.33E-16	1.2E-16	–
187.473 78	7.993 91	6.02E-15	7.74E-16	3.16E-15	4.06E-16	6.35E-15	8.2E-16	2.58E-15	3.34E-16	–
187.473 78	8.044 69	3.28E-15	4.67E-16	1.72E-15	2.45E-16	3.46E-15	4.94E-16	1.41E-15	2.01E-16	–
187.472 34	8.007 24	3.51E-15	4.78E-16	1.84E-15	2.51E-16	3.7E-15	5.06E-16	1.51E-15	2.06E-16	GC
187.472 29	8.0526	3.17E-15	4.43E-16	1.67E-15	2.33E-16	3.35E-15	4.7E-16	1.36E-15	1.91E-16	GC
187.472 28	8.014 91	2.59E-15	3.8E-16	1.36E-15	1.99E-16	2.73E-15	4.02E-16	1.11E-15	1.63E-16	–
187.472 23	7.997 79	3.61E-15	5.01E-16	1.9E-15	2.63E-16	3.81E-15	5.31E-16	1.55E-15	2.16E-16	GC
187.471 44	7.956 63	1.26E-15	3.09E-16	6.61E-16	1.62E-16	1.33E-15	3.27E-16	5.41E-16	1.33E-16	–
187.471 09	7.947 15	1.18E-15	3.36E-16	6.17E-16	1.76E-16	1.24E-15	3.55E-16	5.05E-16	1.44E-16	–
187.470 44	7.991 58	2.18E-15	4.97E-16	1.15E-15	2.61E-16	2.3E-15	5.26E-16	9.36E-16	2.14E-16	–
187.470 31	7.999 06	4.21E-15	5.68E-16	2.21E-15	2.98E-16	4.44E-15	6.01E-16	1.81E-15	2.45E-16	–
187.470 21	7.965 14	1.27E-15	3.67E-16	6.65E-16	1.93E-16	1.34E-15	3.87E-16	5.44E-16	1.58E-16	–
187.470 06	7.972 02	2.93E-15	4.85E-16	1.54E-15	2.55E-16	3.09E-15	5.13E-16	1.26E-15	2.09E-16	GC
187.469 72	8.032 25	1.38E-14	1.62E-15	7.23E-15	8.48E-16	1.45E-14	1.71E-15	5.91E-15	6.97E-16	–
187.469 69	7.952 61	1.78E-15	3.5E-16	9.35E-16	1.84E-16	1.88E-15	3.7E-16	7.64E-16	1.51E-16	GC
187.469 21	8.019 33	1.96E-15	3.07E-16	1.03E-15	1.61E-16	2.06E-15	3.25E-16	8.39E-16	1.32E-16	GC
187.469 14	8.004 49	1.65E-15	3.61E-16	8.67E-16	1.89E-16	1.74E-15	3.81E-16	7.09E-16	1.55E-16	GC
187.468 83	8.000 51	3.14E-15	4.58E-16	1.65E-15	2.41E-16	3.31E-15	4.85E-16	1.35E-15	1.97E-16	GC
187.468 16	7.993 14	3.26E-15	9.31E-16	1.71E-15	4.89E-16	3.43E-15	9.83E-16	1.4E-15	4.0E-16	–
187.467 88	8.012 87	8.14E-16	2.2E-16	4.27E-16	1.15E-16	8.59E-16	2.32E-16	3.49E-16	9.44E-17	–
187.465 82	7.996 76	3.14E-15	9.44E-16	1.65E-15	4.96E-16	3.31E-15	9.97E-16	1.35E-15	4.06E-16	GC
187.465 82	8.039 06	1.48E-15	3.38E-16	7.79E-16	1.77E-16	1.57E-15	3.57E-16	6.37E-16	1.45E-16	cg
187.465 56	7.999 96	4.17E-15	5.69E-16	2.19E-15	2.99E-16	4.4E-15	6.03E-16	1.79E-15	2.45E-16	GC
187.465 48	7.9732	2.56E-15	4.07E-16	1.34E-15	2.13E-16	2.7E-15	4.3E-16	1.1E-15	1.75E-16	–
187.465 43	7.991 96	1.39E-15	3.23E-16	7.27E-16	1.7E-16	1.46E-15	3.41E-16	5.95E-16	1.39E-16	GC
187.465 07	8.000 83	3.99E-15	1.05E-15	2.1E-15	5.5E-16	4.21E-15	1.11E-15	1.71E-15	4.5E-16	–
187.464 89	7.966 36	2.55E-15	4.6E-16	1.34E-15	2.42E-16	2.69E-15	4.87E-16	1.09E-15	1.98E-16	–
187.464 78	7.951 26	2.51E-15	4.85E-16	1.32E-15	2.55E-16	2.65E-15	5.13E-16	1.08E-15	2.09E-16	–
187.46394	7.98809	2.08E-15	3.7E-16	1.09E-15	1.94E-16	2.19E-15	3.91E-16	8.91E-16	1.59E-16	GC
187.4634	8.057 63	3.52E-15	9.38E-16	1.85E-15	4.92E-16	3.72E-15	9.9E-16	1.51E-15	4.03E-16	–
187.463 23	7.974 08	1.04E-15	2.63E-16	5.44E-16	1.38E-16	1.09E-15	2.78E-16	4.45E-16	1.13E-16	–
187.463 15	8.040 35	7.28E-15	9.14E-16	3.82E-15	4.8E-16	7.68E-15	9.69E-16	3.12E-15	3.94E-16	–
187.46276	7.99645	3.37E-15	1.04E-15	1.77E-15	5.46E-16	3.56E-15	1.1E-15	1.45E-15	4.47E-16	GC
187.462 25	7.987 36	1.49E-15	3.46E-16	7.79E-16	1.82E-16	1.57E-15	3.66E-16	6.37E-16	1.49E-16	GC
187.462	8.002 71	9.52E-15	1.14E-15	5.0E-15	6.01E-16	1.0E-14	1.21E-15	4.08E-15	4.93E-16	GC
187.461 96	8.036 52	2.07E-15	3.6E-16	1.09E-15	1.89E-16	2.18E-15	3.81E-16	8.87E-16	1.55E-16	–
187.461 83	7.9715	1.95E-15	3.68E-16	1.02E-15	1.93E-16	2.05E-15	3.89E-16	8.35E-16	1.58E-16	–
187.461 69	8.046 09	1.04E-15	1.99E-16	5.44E-16	1.05E-16	1.09E-15	2.11E-16	4.45E-16	8.58E-17	–
187.461 32	8.019 72	1.18E-15	2.38E-16	6.2E-16	1.25E-16	1.25E-15	2.51E-16	5.07E-16	1.02E-16	GC
187.461 06	7.964 07	2.05E-15	4.9E-16	1.07E-15	2.57E-16	2.16E-15	5.18E-16	8.77E-16	2.11E-16	–
187.461 01	8.006 52	6.63E-16	2.4E-16	3.48E-16	1.26E-16	6.99E-16	2.53E-16	2.84E-16	1.03E-16	–
187.460 63	7.988 88	3.41E-15	4.96E-16	1.79E-15	2.6E-16	3.6E-15	5.25E-16	1.47E-15	2.13E-16	–

Table 3 – *continued*

RA (degrees)	Dec. (degrees)	$Flux_{PL}$ (0.5–5 keV)	$Flux_{PL}$ err (0.5–5 keV)	$Flux_{PL}$ (0.5–2 keV)	$Flux_{PL}$ err (0.5–2 keV)	$Flux_{DBB}$ (0.5–5 keV)	$Flux_{DBB}$ err (0.5–5 keV)	$Flux_{DBB}$ (0.5–2 keV)	$Flux_{DBB}$ err (0.5-2 keV)	Flag
187.460 04	8.003 79	9.21E-15	1.11E-15	4.83E-15	5.82E-16	9.72E-15	1.18E-15	3.95E-15	4.78E-16	GC
187.459 57	8.009 99	1.86E-15	3.42E-16	9.78E-16	1.79E-16	1.97E-15	3.61E-16	8.0E-16	1.47E-16	–
187.4594	7.973 35	1.96E-15	3.71E-16	1.03E-15	1.95E-16	2.06E-15	3.93E-16	8.4E-16	1.6E-16	–
187.458 86	8.021 88	1.45E-15	2.75E-16	7.63E-16	1.45E-16	1.53E-15	2.91E-16	6.24E-16	1.18E-16	–
187.458 78	7.995 47	7.63E-15	9.79E-16	4.0E-15	5.14E-16	8.04E-15	1.04E-15	3.27E-15	4.22E-16	GC
187.457 89	7.999 61	1.86E-15	5.43E-16	9.79E-16	2.85E-16	1.97E-15	5.73E-16	8.0E-16	2.33E-16	bkg
187.457 58	8.007 14	1.07E-15	2.57E-16	5.6E-16	1.35E-16	1.13E-15	2.71E-16	4.58E-16	1.1E-16	–
187.456 39	7.986 17	1.28E-15	3.31E-16	6.74E-16	1.74E-16	1.36E-15	3.5E-16	5.51E-16	1.42E-16	–
187.456 36	7.990 33	1.62E-15	4.87E-16	8.48E-16	2.56E-16	1.7E-15	5.14E-16	6.93E-16	2.09E-16	bkg, GC
187.456 12	7.992 93	1.86E-15	4.04E-16	9.78E-16	2.12E-16	1.97E-15	4.27E-16	8.0E-16	1.74E-16	GC
187.456 08	8.055 66	8.28E-16	1.87E-16	4.34E-16	9.79E-17	8.73E-16	1.97E-16	3.55E-16	8.02E-17	–
187.455 68	7.964 79	5.58E-15	7.49E-16	2.93E-15	3.93E-16	5.88E-15	7.94E-16	2.39E-15	3.23E-16	GC
187.455 52	8.003 58	1.52E-14	1.79E-15	7.98E-15	9.39E-16	1.6E-14	1.9E-15	6.52E-15	7.71E-16	–
187.4555	8.038 52	1.23E-15	2.73E-16	6.46E-16	1.43E-16	1.3E-15	2.89E-16	5.28E-16	1.17E-16	GC
187.455 24	8.029 64	1.96E-15	3.12E-16	1.03E-15	1.64E-16	2.07E-15	3.3E-16	8.41E-16	1.34E-16	–
187.455 09	8.054 76	1.24E-15	3.06E-16	6.52E-16	1.61E-16	1.31E-15	3.23E-16	5.33E-16	1.31E-16	c
187.455 07	8.0155	7.23E-16	2.62E-16	3.8E-16	1.38E-16	7.63E-16	2.77E-16	3.1E-16	1.13E-16	GC
187.454 61	8.0076	8.41E-16	2.18E-16	4.41E-16	1.14E-16	8.87E-16	2.3E-16	3.61E-16	9.36E-17	GC
187.454 38	7.991 98	1.52E-15	4.46E-16	7.95E-16	2.34E-16	1.6E-15	4.7E-16	6.5E-16	1.91E-16	–
187.454 26	7.980 95	1.5E-14	1.76E-15	7.88E-15	9.26E-16	1.58E-14	1.87E-15	6.44E-15	7.61E-16	–
187.454 16	7.996 12	2.81E-15	4.66E-16	1.48E-15	2.45E-16	2.97E-15	4.93E-16	1.21E-15	2.01E-16	–
187.453 79	7.979 48	1.73E-15	4.34E-16	9.07E-16	2.28E-16	1.82E-15	4.59E-16	7.41E-16	1.87E-16	GC
187.453 75	8.016 16	4.87E-16	2.1E-16	2.56E-16	1.1E-16	5.14E-16	2.21E-16	2.09E-16	9.0E-17	–
187.453 08	8.021 45	1.11E-15	3.36E-16	5.84E-16	1.76E-16	1.18E-15	3.55E-16	4.78E-16	1.44E-16	–
187.452 61	7.9984	2.16E-15	4.14E-16	1.13E-15	2.17E-16	2.28E-15	4.38E-16	9.26E-16	1.78E-16	–
187.452 61	7.987 06	1.9E-15	4.38E-16	9.98E-16	2.3E-16	2.01E-15	4.62E-16	8.16E-16	1.88E-16	–
187.4525	7.995 42	5.88E-15	8.37E-16	3.09E-15	4.4E-16	6.2E-15	8.87E-16	2.52E-15	3.61E-16	–
187.451 98	8.009 91	1.55E-15	4.8E-16	8.15E-16	2.52E-16	1.64E-15	5.07E-16	6.66E-16	2.06E-16	bkg
187.451 87	8.033 41	9.42E-16	2.0E-16	4.94E-16	1.05E-16	9.93E-16	2.11E-16	4.04E-16	8.58E-17	–
187.451 55	8.005 54	8.56E-16	3.34E-16	4.49E-16	1.75E-16	9.03E-16	3.52E-16	3.67E-16	1.43E-16	–
187.451 35	7.992 31	3.51E-15	5.81E-16	1.84E-15	3.05E-16	3.7E-15	6.15E-16	1.51E-15	2.5E-16	–
187.451 13	8.004 54	2.89E-15	1.09E-15	1.52E-15	5.74E-16	3.05E-15	1.15E-15	1.24E-15	4.69E-16	–
187.450 73	8.016 39	1.49E-15	2.71E-16	7.79E-16	1.42E-16	1.57E-15	2.86E-16	6.37E-16	1.17E-16	–
187.450 34	7.994 76	1.44E-15	4.38E-16	7.54E-16	2.3E-16	1.52E-15	4.62E-16	6.17E-16	1.88E-16	GC
187.450 09	7.976 28	6.51E-16	2.47E-16	3.42E-16	1.3E-16	6.87E-16	2.61E-16	2.8E-16	1.06E-16	GC
187.450 06	7.985 58	1.54E-15	3.65E-16	8.1E-16	1.92E-16	1.63E-15	3.86E-16	6.62E-16	1.57E-16	–
187.449 82	8.002 33	8.39E-15	1.36E-15	4.4E-15	7.14E-16	8.85E-15	1.44E-15	3.6E-15	5.85E-16	bkg, GC
187.449 47	7.997 76	3.19E-15	7.79E-16	1.67E-15	4.09E-16	3.36E-15	8.23E-16	1.37E-15	3.35E-16	bkg
187.449 46	8.010 21	3.44E-15	5.42E-16	1.81E-15	2.84E-16	3.63E-15	5.73E-16	1.48E-15	2.33E-16	–
187.449 42	7.995 56	1.32E-15	4.35E-16	6.91E-16	2.28E-16	1.39E-15	4.59E-16	5.65E-16	1.87E-16	–
187.449 41	7.988 63	2.18E-15	4.32E-16	1.15E-15	2.27E-16	2.3E-15	4.57E-16	9.36E-16	1.86E-16	GC
187.449 36	7.992 83	2.55E-15	4.88E-16	1.34E-15	2.56E-16	2.69E-15	5.16E-16	1.09E-15	2.1E-16	–
187.4492	8.005 54	1.08E-15	4.19E-16	5.67E-16	2.2E-16	1.14E-15	4.43E-16	4.63E-16	1.8E-16	bkg
187.448 94	7.990 55	4.14E-15	5.99E-16	2.17E-15	3.14E-16	4.37E-15	6.34E-16	1.78E-15	2.58E-16	GC
187.448 81	7.982 98	1.43E-15	3.82E-16	7.51E-16	2.0E-16	1.51E-15	4.03E-16	6.14E-16	1.64E-16	–
187.448 73	8.028 52	1.28E-15	2.5E-16	6.74E-16	1.31E-16	1.35E-15	2.65E-16	5.51E-16	1.08E-16	–
187.448 68	8.021 99	1.49E-15	2.96E-16	7.8E-16	1.55E-16	1.57E-15	3.13E-16	6.38E-16	1.27E-16	–
187.448 67	8.0074	7.79E-15	9.76E-16	4.09E-15	5.12E-16	8.22E-15	1.04E-15	3.34E-15	4.21E-16	–
187.448 49	7.978 68	1.06E-15	2.77E-16	5.54E-16	1.45E-16	1.11E-15	2.92E-16	4.53E-16	1.19E-16	–
187.447 65	8.002 22	1.47E-14	2.0E-15	7.71E-15	1.05E-15	1.55E-14	2.12E-15	6.3E-15	8.61E-16	–
187.447 53	7.986 58	1.1E-15	3.52E-16	5.78E-16	1.85E-16	1.16E-15	3.71E-16	4.72E-16	1.51E-16	GC
187.447 16	8.015 75	1.04E-15	2.41E-16	5.43E-16	1.26E-16	1.09E-15	2.54E-16	4.44E-16	1.04E-16	GC
187.4465	8.038	7.06E-16	2.27E-16	3.7E-16	1.19E-16	7.44E-16	2.4E-16	3.03E-16	9.76E-17	–
187.446 48	7.976 05	1.78E-15	3.49E-16	9.32E-16	1.83E-16	1.87E-15	3.68E-16	7.62E-16	1.5E-16	GC
187.446 04	8.031 01	7.59E-16	1.83E-16	3.98E-16	9.63E-17	8.01E-16	1.94E-16	3.26E-16	7.88E-17	cg
187.446 02	8.003 73	1.91E-14	2.28E-15	1.0E-14	1.2E-15	2.01E-14	2.42E-15	8.19E-15	9.83E-16	–
187.445 98	7.995 39	1.24E-15	4.57E-16	6.53E-16	2.4E-16	1.31E-15	4.83E-16	5.34E-16	1.96E-16	–
187.445 95	7.979 69	5.78E-15	7.48E-16	3.03E-15	3.93E-16	6.1E-15	7.93E-16	2.48E-15	3.22E-16	GC
187.445 17	7.982 95	1.7E-15	3.64E-16	8.91E-16	1.91E-16	1.79E-15	3.85E-16	7.29E-16	1.57E-16	–
187.444 18	7.992 37	2.18E-15	4.25E-16	1.15E-15	2.23E-16	2.3E-15	4.49E-16	9.37E-16	1.83E-16	–
187.443 99	7.990 15	1.97E-15	3.85E-16	1.04E-15	2.02E-16	2.08E-15	4.06E-16	8.46E-16	1.65E-16	–
187.443 64	7.994 37	1.6E-15	4.42E-16	8.38E-16	2.32E-16	1.68E-15	4.66E-16	6.85E-16	1.9E-16	–
187.443 49	8.018 67	1.4E-15	3.69E-16	7.35E-16	1.94E-16	1.48E-15	3.9E-16	6.01E-16	1.59E-16	–

Table 3 – *continued*

RA (degrees)	Dec. (degrees)	$Flux_{PL}$ (0.5–5 keV)	$Flux_{PL}$ err (0.5–5 keV)	$Flux_{PL}$ (0.5–2 keV)	$Flux_{PL}$ err (0.5–2 keV)	$Flux_{DBB}$ (0.5–5 keV)	$Flux_{DBB}$ err (0.5–5 keV)	$Flux_{DBB}$ (0.5–2 keV)	$Flux_{DBB}$ err (0.5-2 keV)	Flag
187.443 35	8.020 61	9.58E-16	2.93E-16	5.03E-16	1.54E-16	1.01E-15	3.09E-16	4.11E-16	1.26E-16	–
187.443 27	7.961 77	1.51E-15	3.77E-16	7.94E-16	1.98E-16	1.6E-15	3.98E-16	6.49E-16	1.62E-16	–
187.443 17	8.024 19	3.13E-15	4.35E-16	1.64E-15	2.28E-16	3.3E-15	4.6E-16	1.34E-15	1.87E-16	GC
187.442 88	7.978 72	2.15E-15	3.95E-16	1.13E-15	2.07E-16	2.26E-15	4.17E-16	9.2E-16	1.7E-16	–
187.442 88	8.022 39	9.69E-16	2.28E-16	5.08E-16	1.2E-16	1.02E-15	2.41E-16	4.16E-16	9.8E-17	–
187.4425	7.998 15	2.88E-14	3.44E-15	1.51E-14	1.8E-15	3.04E-14	3.64E-15	1.23E-14	1.48E-15	–
187.442 31	7.989 61	3.31E-15	5.06E-16	1.74E-15	2.66E-16	3.49E-15	5.35E-16	1.42E-15	2.18E-16	GC
187.442 05	8.023 09	1.15E-15	2.42E-16	6.04E-16	1.27E-16	1.21E-15	2.56E-16	4.94E-16	1.04E-16	GC
187.442 02	7.987 61	1.38E-14	1.64E-15	7.24E-15	8.62E-16	1.46E-14	1.74E-15	5.92E-15	7.08E-16	GC
187.441 31	8.024 14	5.76E-15	7.22E-16	3.02E-15	3.79E-16	6.08E-15	7.66E-16	2.47E-15	3.11E-16	GC
187.440 93	8.004 75	4.39E-15	8.92E-16	2.3E-15	4.68E-16	4.63E-15	9.43E-16	1.88E-15	3.84E-16	–
187.440 87	7.988 51	2.84E-15	5.14E-16	1.49E-15	2.7E-16	3.0E-15	5.43E-16	1.22E-15	2.21E-16	–
187.440 78	7.962 04	2.82E-15	5.15E-16	1.48E-15	2.7E-16	2.98E-15	5.44E-16	1.21E-15	2.21E-16	GC
187.4406	7.9692	3.14E-15	4.77E-16	1.65E-15	2.51E-16	3.31E-15	5.05E-16	1.35E-15	2.05E-16	–
187.440 54	8.024 76	2.58E-15	3.77E-16	1.35E-15	1.98E-16	2.72E-15	3.99E-16	1.11E-15	1.62E-16	c
187.440 23	7.994 62	1.04E-15	3.31E-16	5.44E-16	1.74E-16	1.09E-15	3.49E-16	4.45E-16	1.42E-16	GC
187.440 04	7.993 41	7.4E-16	2.68E-16	3.89E-16	1.41E-16	7.81E-16	2.83E-16	3.18E-16	1.15E-16	GC
187.439 88	8.024 79	2.35E-15	3.58E-16	1.24E-15	1.88E-16	2.48E-15	3.79E-16	1.01E-15	1.54E-16	c
187.439 85	8.0164	6.02E-15	7.61E-16	3.16E-15	4.0E-16	6.35E-15	8.07E-16	2.58E-15	3.28E-16	–
187.439 68	8.033 74	3.11E-15	4.28E-16	1.63E-15	2.25E-16	3.28E-15	4.54E-16	1.33E-15	1.85E-16	–
187.439 41	7.991 74	2.56E-15	4.79E-16	1.34E-15	2.52E-16	2.7E-15	5.07E-16	1.1E-15	2.06E-16	–
187.4392	7.985 76	2.35E-15	5.29E-16	1.23E-15	2.78E-16	2.48E-15	5.59E-16	1.01E-15	2.27E-16	–
187.439 19	7.987 81	1.87E-15	4.26E-16	9.81E-16	2.24E-16	1.97E-15	4.5E-16	8.02E-16	1.83E-16	–
187.4391	7.993 42	1.71E-15	3.85E-16	8.98E-16	2.02E-16	1.81E-15	4.07E-16	7.35E-16	1.66E-16	GC
187.439	8.0046	7.38E-15	9.98E-16	3.87E-15	5.24E-16	7.78E-15	1.06E-15	3.17E-15	4.3E-16	–
187.438 99	7.994 49	2.04E-15	4.14E-16	1.07E-15	2.17E-16	2.15E-15	4.37E-16	8.74E-16	1.78E-16	GC
187.438 93	8.008 17	1.99E-15	3.85E-16	1.04E-15	2.02E-16	2.1E-15	4.07E-16	8.52E-16	1.65E-16	–
187.438 46	8.025 02	4.56E-16	1.96E-16	2.39E-16	1.03E-16	4.81E-16	2.07E-16	1.96E-16	8.42E-17	–
187.438 25	7.947 48	1.69E-15	4.53E-16	8.87E-16	2.38E-16	1.78E-15	4.79E-16	7.25E-16	1.95E-16	–
187.438 23	8.010 61	4.85E-16	2.33E-16	2.55E-16	1.22E-16	5.12E-16	2.46E-16	2.08E-16	1.0E-16	bkg
187.437 63	7.997 41	3.48E-15	5.13E-16	1.82E-15	2.69E-16	3.67E-15	5.43E-16	1.49E-15	2.21E-16	GC
187.437 55	8.036 82	1.95E-15	3.24E-16	1.03E-15	1.7E-16	2.06E-15	3.42E-16	8.38E-16	1.39E-16	–
187.437 33	8.010 12	9.53E-16	3.29E-16	5.0E-16	1.73E-16	1.01E-15	3.47E-16	4.09E-16	1.41E-16	bkg
187.4368	8.0013	1.96E-15	3.7E-16	1.03E-15	1.94E-16	2.07E-15	3.91E-16	8.41E-16	1.59E-16	–
187.436 75	8.059 09	1.08E-15	2.89E-16	5.68E-16	1.52E-16	1.14E-15	3.05E-16	4.64E-16	1.24E-16	–
187.4361	8.000 19	4.43E-15	6.12E-16	2.33E-15	3.21E-16	4.68E-15	6.48E-16	1.9E-15	2.64E-16	–
187.435 83	7.956 21	2.79E-15	5.13E-16	1.46E-15	2.69E-16	2.94E-15	5.42E-16	1.2E-15	2.21E-16	–
187.434 94	8.039 65	9.25E-16	3.23E-16	4.86E-16	1.7E-16	9.76E-16	3.41E-16	3.97E-16	1.39E-16	–
187.434 83	7.994 99	9.4E-16	3.1E-16	4.93E-16	1.63E-16	9.92E-16	3.27E-16	4.03E-16	1.33E-16	GC
187.434 15	8.011 61	3.25E-15	4.72E-16	1.71E-15	2.48E-16	3.43E-15	5.0E-16	1.4E-15	2.03E-16	GC
187.433 95	8.056 97	1.14E-15	3.08E-16	5.99E-16	1.62E-16	1.2E-15	3.26E-16	4.9E-16	1.32E-16	–
187.433 75	7.978 04	6.34E-15	8.32E-16	3.33E-15	4.37E-16	6.69E-15	8.82E-16	2.72E-15	3.59E-16	GC
187.433 43	8.020 91	1.92E-15	6.93E-16	1.01E-15	3.64E-16	2.03E-15	7.31E-16	8.24E-16	2.98E-16	GC
187.433 32	7.997 64	5.77E-15	7.61E-16	3.03E-15	4.0E-16	6.09E-15	8.06E-16	2.48E-15	3.28E-16	GC
187.433 02	8.047 08	9.81E-15	1.74E-15	5.15E-15	9.14E-16	1.04E-14	1.84E-15	4.21E-15	7.49E-16	–
187.432 89	8.053 09	6.23E-16	2.13E-16	3.27E-16	1.12E-16	6.57E-16	2.24E-16	2.67E-16	9.13E-17	–
187.432 69	7.965 69	3.06E-15	6.56E-16	1.6E-15	3.44E-16	3.22E-15	6.93E-16	1.31E-15	2.82E-16	GC
187.432 59	7.999 11	1.52E-15	3.26E-16	8.0E-16	1.71E-16	1.61E-15	3.45E-16	6.54E-16	1.4E-16	GC
187.432 48	7.9543	4.08E-15	5.94E-16	2.14E-15	3.12E-16	4.31E-15	6.29E-16	1.75E-15	2.56E-16	–
187.432 45	7.958 42	1.88E-15	4.22E-16	9.89E-16	2.21E-16	1.99E-15	4.46E-16	8.08E-16	1.81E-16	–
187.432 37	8.011 62	2.42E-15	4.0E-16	1.27E-15	2.1E-16	2.56E-15	4.23E-16	1.04E-15	1.72E-16	GC
187.431 85	8.014 42	3.08E-15	4.39E-16	1.62E-15	2.31E-16	3.25E-15	4.65E-16	1.32E-15	1.89E-16	–
187.431 42	7.981 88	1.25E-15	3.45E-16	6.57E-16	1.81E-16	1.32E-15	3.65E-16	5.37E-16	1.48E-16	–
187.431 35	7.996 51	9.21E-15	1.13E-15	4.83E-15	5.95E-16	9.71E-15	1.2E-15	3.95E-15	4.88E-16	–
187.431 02	8.032 89	3.25E-15	1.37E-15	1.7E-15	7.2E-16	3.42E-15	1.45E-15	1.39E-15	5.89E-16	–
187.430 47	8.060 57	2.41E-15	3.56E-16	1.26E-15	1.87E-16	2.54E-15	3.77E-16	1.03E-15	1.53E-16	–
187.430 35	8.043 47	3.95E-15	1.06E-15	2.07E-15	5.54E-16	4.17E-15	1.12E-15	1.7E-15	4.54E-16	cg
187.429 99	7.981 77	8.77E-16	3.02E-16	4.6E-16	1.58E-16	9.25E-16	3.18E-16	3.76E-16	1.3E-16	–
187.429 88	8.009 11	1.64E-15	3.32E-16	8.58E-16	1.74E-16	1.73E-15	3.51E-16	7.02E-16	1.43E-16	–
187.429 51	8.011 01	4.92E-15	6.43E-16	2.58E-15	3.37E-16	5.19E-15	6.81E-16	2.11E-15	2.77E-16	GC
187.429 38	8.038 32	5.66E-16	2.04E-16	2.97E-16	1.07E-16	5.97E-16	2.15E-16	2.43E-16	8.74E-17	–
187.429 23	7.982 38	1.66E-15	4.28E-16	8.71E-16	2.24E-16	1.75E-15	4.52E-16	7.12E-16	1.84E-16	–
187.429 22	7.957 75	1.85E-15	4.78E-16	9.73E-16	2.51E-16	1.96E-15	5.04E-16	7.95E-16	2.05E-16	–

Table 3 – *continued*

RA (degrees)	Dec. (degrees)	$Flux_{PL}$ (0.5–5 keV)	$Flux_{PL}$ err (0.5–5 keV)	$Flux_{PL}$ (0.5–2 keV)	$Flux_{PL}$ err (0.5–2 keV)	$Flux_{DBB}$ (0.5–5 keV)	$Flux_{DBB}$ err (0.5–5 keV)	$Flux_{DBB}$ (0.5–2 keV)	$Flux_{DBB}$ err (0.5-2 keV)	Flag
187.429 11	7.979 57	2.74E-15	4.24E-16	1.44E-15	2.23E-16	2.89E-15	4.49E-16	1.18E-15	1.82E-16	GC
187.427 65	8.044 81	1.11E-15	2.89E-16	5.81E-16	1.52E-16	1.17E-15	3.06E-16	4.75E-16	1.24E-16	cg
187.426 39	8.002 18	2.38E-14	2.74E-15	1.25E-14	1.44E-15	2.51E-14	2.91E-15	1.02E-14	1.18E-15	GC
187.426 24	8.025 24	8.39E-16	2.54E-16	4.4E-16	1.33E-16	8.85E-16	2.68E-16	3.6E-16	1.09E-16	–
187.426 03	7.950 57	1.93E-14	2.25E-15	1.01E-14	1.18E-15	2.04E-14	2.39E-15	8.29E-15	9.71E-16	–
187.425 09	8.003 96	3.43E-15	9.75E-16	1.8E-15	5.12E-16	3.62E-15	1.03E-15	1.47E-15	4.19E-16	–
187.425 09	7.984 77	2.25E-15	5.92E-16	1.18E-15	3.11E-16	2.37E-15	6.25E-16	9.64E-16	2.54E-16	–
187.424 93	7.980 13	8.64E-15	1.07E-15	4.54E-15	5.6E-16	9.12E-15	1.13E-15	3.71E-15	4.59E-16	–
187.4247	8.021 68	1.21E-15	5.16E-16	6.37E-16	2.71E-16	1.28E-15	5.45E-16	5.21E-16	2.22E-16	–
187.423 71	7.972 53	2.65E-15	5.3E-16	1.39E-15	2.78E-16	2.8E-15	5.6E-16	1.14E-15	2.28E-16	–
187.4236	8.000 46	1.14E-15	3.1E-16	5.99E-16	1.63E-16	1.2E-15	3.28E-16	4.9E-16	1.33E-16	GC
187.4235	8.013 64	1.25E-15	2.45E-16	6.57E-16	1.29E-16	1.32E-15	2.59E-16	5.37E-16	1.05E-16	GC
187.423 42	8.017 31	2.82E-15	4.04E-16	1.48E-15	2.12E-16	2.97E-15	4.28E-16	1.21E-15	1.74E-16	–
187.423 42	8.012 38	1.76E-15	3.02E-16	9.25E-16	1.58E-16	1.86E-15	3.19E-16	7.57E-16	1.3E-16	GC
187.423 36	8.003 98	9.62E-15	1.18E-15	5.05E-15	6.17E-16	1.01E-14	1.25E-15	4.13E-15	5.07E-16	GC
187.423 34	8.016 33	4.79E-15	6.26E-16	2.51E-15	3.29E-16	5.05E-15	6.63E-16	2.06E-15	2.7E-16	GC
187.423 06	7.975 56	3.5E-15	5.1E-16	1.84E-15	2.68E-16	3.7E-15	5.4E-16	1.5E-15	2.2E-16	–
187.422 66	7.984 55	5.57E-15	7.27E-16	2.93E-15	3.82E-16	5.88E-15	7.7E-16	2.39E-15	3.13E-16	–
187.422 55	7.981 66	4.62E-15	6.39E-16	2.43E-15	3.35E-16	4.88E-15	6.77E-16	1.98E-15	2.75E-16	–
187.422 49	8.035 55	1.3E-15	2.43E-16	6.8E-16	1.27E-16	1.37E-15	2.57E-16	5.56E-16	1.04E-16	–
187.422 42	7.957 37	4.76E-15	6.81E-16	2.5E-15	3.58E-16	5.03E-15	7.22E-16	2.04E-15	2.93E-16	–
187.421 64	7.991 88	1.54E-15	3.51E-16	8.09E-16	1.84E-16	1.63E-15	3.71E-16	6.61E-16	1.51E-16	–
187.420 92	8.000 86	3.26E-15	4.77E-16	1.71E-15	2.5E-16	3.44E-15	5.05E-16	1.4E-15	2.05E-16	GC
187.420 88	7.962 33	5.11E-14	5.78E-15	2.68E-14	3.03E-15	5.39E-14	6.13E-15	2.19E-14	2.49E-15	GC
187.420 39	7.995 27	4.64E-15	6.21E-16	2.43E-15	3.26E-16	4.89E-15	6.58E-16	1.99E-15	2.68E-16	–
187.418 45	8.040 04	1.04E-15	2.24E-16	5.45E-16	1.18E-16	1.1E-15	2.37E-16	4.45E-16	9.64E-17	–
187.4175	7.9957	2.84E-15	4.44E-16	1.49E-15	2.33E-16	3.0E-15	4.7E-16	1.22E-15	1.91E-16	GC
187.417 45	7.9748	3.9E-15	1.23E-15	2.04E-15	6.46E-16	4.11E-15	1.3E-15	1.67E-15	5.29E-16	GC
187.417 07	7.990 93	7.94E-15	9.78E-16	4.16E-15	5.13E-16	8.37E-15	1.04E-15	3.41E-15	4.22E-16	GC
187.415 36	7.982 63	1.33E-15	3.34E-16	6.99E-16	1.75E-16	1.41E-15	3.53E-16	5.72E-16	1.43E-16	GC
187.415 24	7.991 26	1.67E-15	3.86E-16	8.76E-16	2.03E-16	1.76E-15	4.08E-16	7.16E-16	1.66E-16	GC
187.4145	8.028 78	3.73E-15	5.16E-16	1.96E-15	2.71E-16	3.93E-15	5.46E-16	1.6E-15	2.22E-16	–
187.414 33	8.010 41	1.96E-15	3.36E-16	1.03E-15	1.77E-16	2.07E-15	3.56E-16	8.43E-16	1.45E-16	–
187.413 24	7.988 68	5.07E-15	6.78E-16	2.66E-15	3.56E-16	5.35E-15	7.19E-16	2.18E-15	2.92E-16	GC
187.413 14	7.994 75	2.74E-15	4.25E-16	1.44E-15	2.23E-16	2.9E-15	4.5E-16	1.18E-15	1.83E-16	GC
187.412 75	7.953 64	3.95E-15	6.24E-16	2.07E-15	3.28E-16	4.16E-15	6.6E-16	1.69E-15	2.69E-16	GC
187.411 18	7.965 51	5.0E-15	7.05E-16	2.62E-15	3.7E-16	5.27E-15	7.47E-16	2.15E-15	3.04E-16	GC
187.410 49	8.040 92	9.77E-16	2.48E-16	5.13E-16	1.3E-16	1.03E-15	2.62E-16	4.19E-16	1.06E-16	–
187.410 46	7.991 52	1.84E-15	6.81E-16	9.68E-16	3.58E-16	1.95E-15	7.19E-16	7.92E-16	2.92E-16	GC
187.409 74	8.008 33	4.49E-15	5.95E-16	2.36E-15	3.13E-16	4.74E-15	6.31E-16	1.93E-15	2.57E-16	–
187.409 46	8.003 56	1.14E-15	2.68E-16	5.98E-16	1.41E-16	1.2E-15	2.84E-16	4.89E-16	1.15E-16	GC
187.409 14	8.042 96	3.24E-15	4.74E-16	1.7E-15	2.49E-16	3.42E-15	5.02E-16	1.39E-15	2.04E-16	–
187.408 86	7.977 14	4.37E-15	7.0E-16	2.29E-15	3.67E-16	4.61E-15	7.4E-16	1.88E-15	3.01E-16	–
187.407 46	7.979 34	9.39E-15	1.17E-15	4.93E-15	6.16E-16	9.91E-15	1.24E-15	4.03E-15	5.06E-16	GC
187.407 31	8.012 71	4.22E-15	5.72E-16	2.21E-15	3.0E-16	4.45E-15	6.06E-16	1.81E-15	2.46E-16	–
187.406 54	8.021 18	1.26E-15	2.86E-16	6.61E-16	1.5E-16	1.33E-15	3.02E-16	5.41E-16	1.23E-16	–
187.400 84	7.969 44	2.1E-15	5.37E-16	1.1E-15	2.82E-16	2.21E-15	5.67E-16	9.0E-16	2.31E-16	–
187.400 01	8.041 56	1.13E-15	3.29E-16	5.95E-16	1.73E-16	1.2E-15	3.47E-16	4.86E-16	1.41E-16	–
187.399 89	8.015 16	1.82E-15	3.28E-16	9.54E-16	1.72E-16	1.92E-15	3.47E-16	7.8E-16	1.41E-16	–
187.396 35	7.999 97	1.59E-15	4.39E-16	8.33E-16	2.3E-16	1.67E-15	4.63E-16	6.81E-16	1.88E-16	–
187.395 64	8.013 46	4.68E-15	6.13E-16	2.46E-15	3.22E-16	4.94E-15	6.5E-16	2.01E-15	2.64E-16	–
187.386 48	7.982 49	9.36E-15	1.17E-15	4.91E-15	6.14E-16	9.87E-15	1.24E-15	4.02E-15	5.04E-16	–
187.386 16	7.982 17	1.31E-14	1.75E-15	6.88E-15	9.21E-16	1.38E-14	1.86E-15	5.62E-15	7.56E-16	–

The XSPEC *goodness* command was used to calculate the goodness-of-fit, using the Anderson–Darling (AD) test statistic, as this test is sensitive to differences between the model and the data at the edges of the distribution (see e.g. Maccarone et al. 2016). We ran 10 000 simulations with the *goodness* command to determine the null hypothesis probability. We find that our XLF data is well fitted with a single PL model, with a null hypothesis probability of 0.24.

Other studies have found that the XLF for LMXBs in elliptical galaxies are better fitted with a broken PL function due to a flattening of the luminosity distribution at low luminosities ($L_X \lesssim 4 \times 10^{37}$ erg s^{-1}; e.g. Voss & Gilfanov 2006). Gilfanov (2004) suggested that this flattening is a ubiquitous property of the XLF for LMXBs. In the case of NGC 4472 itself, Kundu et al. (2002) found that the XLF required a broken PL fit with a break at $L_X = 3 \times 10^{38}$ erg s^{-1}. This break is also seen in the XLF of other galaxies and

it was suggested that this break corresponds to the transition in the XLF from neutron star to black hole binary luminosities (Sarazin, Irwin & Bregman 2000).

We also fit the XLF with a broken PL model, using the same fit statistic and AGN contamination component as for the single PL. The best-fitting parameters for the broken PL are as follows: the slope values are $1.34^{+0.43}_{-0.55}$ and $2.60^{+0.55}_{-0.37}$ for the low and high luminosity range of the XLF, with a normalization of $93.99^{+34.30}_{-19.43}$. The break energy is found to be $1.19^{+0.83}_{-0.36}$ keV. The *goodness* command was used again with the AD test statistic; the null hypothesis was to be 0.04 per cent. This result indicates that the broken PL model is overfitting the data and the added complication of a broken PL model is not justified.

Therefore, since we find an acceptable fit to the data with only a single PL model, we do not consider a broken PL to be necessary to describe the XLF of NGC 4472. Indeed, Kim et al. (2006) showed that the flattening of the XLF slope at low luminosities is not seen in their ensemble of galaxy XLFs. They caution against the acceptance of the flattening as a general characteristic of the XLF across all galaxies, since factors such as incompleteness and multiple X-ray point source populations may not have been taken into account in other studies. We note that NGC 4472 does not have multiple point source populations and we only use completeness limited sample, with ∼100 sources less luminous than 10^{38} erg s^{-1}, to construct our XLF.

3.2 Globular cluster LMXB population

We find that a total of 80 of the 238 detected X-ray sources are associated with GCs, 68 with fluxes above the X-ray completeness limit. The X-ray and optical parameter values of these 80 sources can be found in Table 4. A total of 233 X-ray sources lie within the RZ01 survey field and of these 40 were found to have a match with a RZ01 GC, with a subsample of 35 with fluxes above the X-ray completeness limit. The VCS field included 210 X-ray sources and 56 matches were found with this data, 46 of which have fluxes above the X-ray completeness limit. Cross matching the MKZ03 GC–LMXB catalogue yielded 24 sources that were matched to a X-ray source in our catalogue, with 23 sources above the X-ray completeness limit. Three of these MKZ03 GC matches were not found in either the VCS or RZ01 catalogues. We estimate that there would be two and five false matches in the RZ01 and VCS samples, respectively.

For the purposes of our analysis, we apply X-ray and optical (see Section 3.2.2) completeness cuts to our GC sample. A comparison of the RZ01 and VCS catalogues show that only 36 per cent of RZ01 GC sources are also found in the VCS catalogue in their overlapping region. Thus we also limit our analysis to field and GC sources that fall within the area covered by the VCS catalogue to ensure a cleaner sample of both GC and field sources for comparison. After applying these three cuts, we have a sample of 44 GC and 89 field LMXBs.

3.2.1 Field versus globular cluster LMXB populations

We compare the GC and field LMXB populations to ascertain whether the two populations have significantly different X-ray properties. We find that there is not statistically significant difference between the mean 0.5–5 keV luminosity for the GC–LMXB 1.1±21.1 × 10^{38} erg s^{-1} and field LMXB populations 1.2±1.3 × 10^{38} erg s^{-1}. These values and findings are consistent with those found by Kundu et al. (2002) for their smaller sample of NGC 4472 LMXBs.

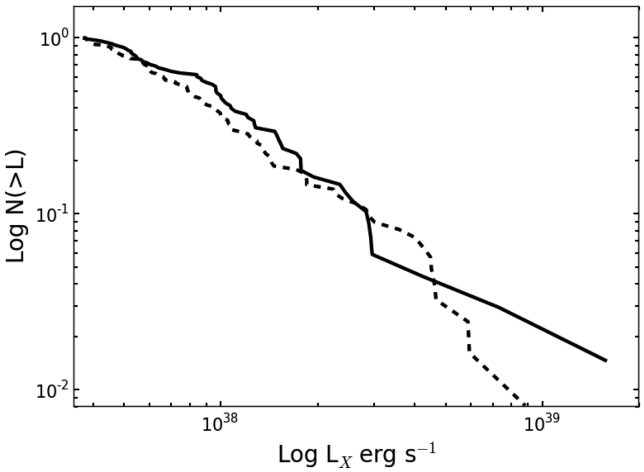

Figure 3. The log N–log L plots for the GC (solid line) and field (dashed line) populations. The number of sources in each sample has been normalized to one for ease of comparison.

The AD test was performed on the luminosities of the GC and field samples to quantify any differences between the two distributions. We find that the probability that the GC and field LMXB luminosities are drawn from the same sample is at least 25 per cent. The findings of previous studies of other elliptical galaxies (see e.g. Kim et al. 2006) as well as that of the previous study of NGC 4472 (Kundu et al. 2002) do not find any significant difference between the two luminosity distributions. Fig. 3 shows the normalized log N–log S plots for both the GC and field LMXB populations.

However, we note that our completeness limit is 3.7 × 10^{37} erg s^{-1} and therefore we do not sample the same low luminosity range as other studies. For example, using samples with completeness limits $\lesssim 10^37$ erg s^{-1}, Voss et al. (2009), Kim et al. (2009) and Zhang et al. (2011) find that the luminosity functions for field and GC–LMXB populations differ significantly for sources with $L_X \lesssim 4 \times 10^{37}$ erg s^{-1}, with fewer faint sources in the GC population. It is then perhaps not surprising that we do not see the flattening of the XLF slope at low luminosities since our completeness limited sample contains very few sources fainter than 4 × 10^{37} erg s^{-1}.

In addition, Lehmer et al. (2014) and Peacock & Zepf (2016) find a flatter slope for the XLF of the GC–LMXB population compared to that of the field population, which implies a difference between the XLFs at the bright end of the distribution as well. We performed an AD test on just the bright ($L_X > 10^{38}$ erg s^{-1}) end of our GC and field luminosity distributions and find that the probability that the GC and field bright end XLFs are statistically similar is at least 25 per cent. Thus our findings are that the field and GC–LMXB luminosity distributions are statistically indistinguishable, which is in contrast to the findings of other studies.

The radial distance distributions of the GC and field LMXB populations were also analysed. For the GC source list, both X-ray and optical completeness was taken into account (see next section for optical completeness data). The average radial distance of field and GC sources was found to be 1.3±0.7 arcmin and 1.5±0.6 arcmin, respectively. We perform an AD test and find the probability that the two radial distance distributions are drawn from the same sample to be 14 per cent. This result is similar to that of Kundu et al. (2002) who found that the probability that the GC and field sources were drawn from the same radial distribution population could not be ruled out at greater than the 30 per cent level.

Table 4. The X-ray and optical properties of the GC LMXBs. The X-ray flux and luminosity are for the 0.5–5 keV range. The X, VCS, RZ and MKZ subscripts denote the RA and Dec. for X-ray, RZ01, VCS and MKZ03 observations, respectively. z and g are the photometric values of the sources in the VCS catalogue; B, V and R are the photometric values of the RZ01 catalogue and V_{MKZ} and I are the photometric values for the MKZ03 catalogue.

RA_X (degrees)	$Dec._X$ (degrees)	$Flux_{PL}$ (0.5-5 keV)	L_X	Flag	RA_{VCS} (degrees)	$Dec._{VCS}$ (degrees)	z	g	g-z	RA_{RZ} (degrees)	$Dec._{RZ}$ (degrees)	V_{RZ}	B-V_{RZ}	V_{RZ}-R	B-R	RA_{MKZ} (degrees)	Dec.mkz03 (degrees)	V_{MKZ}	I	V_{MKZ}-I
187.417 45	7.9748	3.9E-15	1.19E38	–	–	–	–	–	–	187.417 65	7.974 99	22.62	0.66	0.47	1.13	187.4175	7.975	22.77	21.8	0.97
187.420 92	8.000 86	3.26E-15	9.98E37	–	187.420 84	8.000 83	20.9	22.29	1.4	187.421 01	8.001 03	21.89	0.73	0.54	1.27	187.420 83	8.001 03	21.88	20.61	1.26
187.423 36	8.003 98	9.62E-15	2.95E38	–	187.423 25	8.003 92	21.84	23.38	1.53	187.423 37	8.0041	22.88	1.21	0.55	1.76	187.423 33	8.004 11	22.88	21.56	1.32
187.423 42	8.012 38	1.76E-15	5.39E37	–	187.423 35	8.012 32	20.62	22.05	1.44	–	–	–	–	–	–	187.423 33	8.012 53	21.64	20.37	1.27
187.423 34	8.016 33	4.79E-15	1.47E38	–	–	–	–	–	–	–	–	–	–	–	–	187.423 33	8.0165	23.11	22.26	0.85
187.429 51	8.011 01	4.92E-15	1.51E38	–	187.429 31	8.010 97	20.45	21.5	1.05	187.429 45	8.011 16	21.13	0.68	0.45	1.13	187.429 58	8.011 17	21.11	20.1	1.01
187.432 59	7.999 11	1.52E-15	4.65E37	–	187.432 51	7.999 04	20.42	21.61	1.2	–	–	–	–	–	–	187.4325	7.99925	21.12	20.02	1.11
187.432 37	8.011 62	2.42E-15	7.41E37	–	–	–	–	–	–	–	–	–	–	–	–	187.4325	8.011 53	21.2	19.9	1.29
187.433 32	7.997 64	5.77E-15	1.77E38	–	187.433 24	7.997 57	22.26	23.61	1.35	–	–	–	–	–	–	187.433 33	7.997 78	23.19	21.92	1.27
187.434 15	8.011 61	3.25E-15	9.95E37	–	187.434 05	8.011 59	19.95	21.38	1.43	–	–	–	–	–	–	187.434 17	8.011 81	20.86	19.62	1.24
187.440 78	7.962 04	2.82E-15	8.63E37	–	–	–	–	–	–	187.440 91	7.962 26	21.41	0.97	0.59	1.56	187.440 83	7.962 25	21.6	20.29	1.31
187.442 02	7.987 61	1.38E-14	4.23E38	–	–	–	–	–	–	–	–	–	–	–	–	187.442 08	7.987 75	23.83	22.48	1.35
187.443 17	8.024 19	3.13E-15	9.58E37	–	187.44308	8.024 04	23.48	24.68	1.2	–	–	–	–	–	–	187.443 33	8.024 25	24.17	23.12	1.05
187.445 95	7.979 69	5.78E-15	1.77E38	–	187.44588	7.979 61	20.85	22.27	1.43	–	–	–	–	–	–	187.445 83	7.979 83	21.79	20.55	1.24
187.448 94	7.990 55	4.14E-15	1.27E38	–	187.44886	7.990 43	21.74	23.23	1.49	–	–	–	–	–	–	187.449 17	7.990 64	22.63	21.36	1.26
187.449 41	7.988 63	2.18E-15	6.67E37	–	187.4494	7.988 57	20.5	21.85	1.35	187.449 54	7.988 79	21.62	0.59	0.48	1.07	187.449 58	7.988 78	21.33	20.13	1.2
187.454 61	8.0076	8.41E-16	2.57E37	–	187.454 49	8.007 53	22.08	23.42	1.34	–	–	–	–	–	–	187.454 58	8.007 75	22.9	21.73	1.17
187.455 68	7.964 79	5.58E-15	1.71E38	–	–	–	–	–	–	187.455 72	7.964 97	20.82	0.71	0.52	1.23	187.455 83	7.965	21.0	20.0	1.0
187.458 78	7.995 47	7.63E-15	2.34E38	–	187.458 78	7.995 39	20.6	21.75	1.15	187.458 92	7.9956	21.3	0.76	0.51	1.27	187.458 75	7.995 61	21.41	20.28	1.13
187.460 04	8.003 79	9.21E-15	2.82E38	–	187.459 94	8.003 74	20.16	21.71	1.55	187.460 08	8.003 96	21.2	0.88	0.56	1.44	187.46	8.003 94	21.26	19.96	1.3
187.462	8.00271	9.52E-15	2.91E38	–	187.4619	8.002 69	22.7	24.12	1.42	–	–	–	–	–	–	187.462 08	8.002 89	23.61	22.45	1.16
187.463 94	7.988 09	2.08E-15	6.37E37	–	–	–	–	–	–	187.463 97	7.988 23	21.99	0.85	0.54	1.39	187.464 17	7.988 25	21.75	20.57	1.18
187.465 56	7.999 96	4.17E-15	1.28E38	–	187.465 46	7.999 93	19.36	20.8	1.44	–	–	–	–	–	–	187.465 42	8.000 14	20.39	19.14	1.25
187.468 83	8.000 51	3.14E-15	9.61E37	–	187.468 73	8.000 45	22.63	24.2	1.57	–	–	–	–	–	–	187.468 75	8.000 67	23.56	22.35	1.21
187.407 46	7.979 34	9.39E-15	2.87E38	–	–	–	–	–	–	187.407 52	7.979 47	22.03	0.75	0.49	1.24	–	–	–	–	–
187.411 18	7.965 51	5E-15	1.53E38	–	–	–	–	–	–	187.41133	7.965 65	22.94	0.84	0.42	1.26	–	–	–	–	–
187.412 75	7.953 64	3.95E-15	1.21E38	–	–	–	–	–	–	187.412 84	7.953 71	21.43	0.86	0.55	1.41	–	–	–	–	–
187.413 24	7.988 68	5.07E-15	1.55E38	–	187.413 09	7.988 74	19.91	21.29	1.38	187.413 27	7.988 94	20.88	0.79	0.57	1.36	–	–	–	–	–
187.4175	7.9957	2.84E-15	8.7E37	–	187.417 42	7.995 64	19.92	21.23	1.31	187.41 76	7.995 83	20.82	0.8	0.56	1.36	–	–	–	–	–
187.420 88	7.962 33	5.11E-14	1.56E39	–	–	–	–	–	–	187.420 96	7.962 46	21.55	0.85	0.59	1.44	–	–	–	–	–
187.4235	8.013 64	1.25E-15	3.83E37	–	187.4234	8.013 64	21.3	22.33	1.04	187.423 56	8.013 84	22.06	0.46	0.34	0.8	–	–	–	–	–
187.4236	8.000 46	1.14E-15	3.49E37	–	187.423 52	8.000 44	19.84	21.51	1.67	187.423 69	8.000 65	21.01	0.95	0.61	1.56	–	–	–	–	–
187.426 39	8.002 18	2.38E-14	7.29E38	–	187.426 31	8.002 14	19.57	21.0	1.43	187.426 47	8.002 33	20.55	0.82	0.55	1.37	–	–	–	–	–
187.429 11	7.979 57	2.74E-15	8.39E37	–	187.429 01	7.979 48	20.36	21.72	1.36	187.429 18	7.979 69	21.23	0.85	0.44	1.29	–	–	–	–	–
187.432 69	7.965 69	3.06E-15	9.37E37	–	–	–	–	–	–	187.432 94	7.965 93	20.59	0.87	0.54	1.41	–	–	–	–	–
187.446 48	7.976 05	1.78E-15	5.45E37	–	187.446 34	7.976 04	20.59	22.25	1.66	187.4465	7.976 25	21.69	0.83	0.56	1.39	–	–	–	–	–
187.447 16	8.015 75	1.04E-15	3.18E37	–	187.447 01	8.015 79	20.41	21.62	1.2	187.447 18	8.016 01	21.41	0.66	0.55	1.21	–	–	–	–	–
187.447 53	7.986 58	1.1E-15	3.37E37	–	187.447 36	7.986 46	21.26	22.64	1.39	187.447 52	7.986 68	22.47	0.63	0.36	0.99	–	–	–	–	–
187.450 09	7.976 28	6.51E-16	1.99E37	–	187.449 92	7.976 34	20.41	21.7	1.29	187.450 09	7.976 57	21.371	0.71	0.43	1.14	–	–	–	–	–
187.455 07	8.0155	7.23E-16	2.21E37	–	187.454 93	8.015 41	20.37	21.87	1.49	187.4551	8.015 61	21.54	0.73	0.57	1.3	–	–	–	–	–
187.4555	8.038 52	1.23E-15	3.77E37	–	–	–	–	–	–	187.455 59	8.038 69	20.59	0.86	0.59	1.45	–	–	–	–	–

Table 4 – *continued*

RA_X (degrees)	$Dec._X$ (degrees)	$Flux_{PL}$ (0.5-5 keV)	L_X	Flag	RA_{VCS} (degrees)	$Dec._{VCS}$ (degrees)	z	g	g-z	RA_{RZ} (degrees)	$Dec._{RZ}$ (degrees)	V_{RZ}	B-V_{RZ}	V_{RZ}-R	B-R	RA_{MKZ} (degrees)	Dec.mkz03 (degrees)	V_{MKZ}	I	V_{MKZ}-I
187.456 36	7.990 33	1.62E-15	4.96E37	bkg	187.456 33	7.990 25	20.55	22.05	1.5	187.456 52	7.990 47	21.81	0.88	0.65	1.53	–	–	–	–	–
187.462 76	7.996 45	3.37E-15	1.03E38	–	187.462 86	7.996 32	19.81	21.28	1.48	187.463 03	7.996 54	20.98	0.88	0.57	1.45	–	–	–	–	–
187.469 14	8.004 49	1.65E-15	5.05E37	–	187.469 01	8.004 49	20.67	22.12	1.45	187.469 17	8.004 67	21.77	0.8	0.55	1.35	–	–	–	–	–
187.469 69	7.952 61	1.78E-15	5.45E37	–	–	–	–	–	–	187.469 81	7.952 84	21.82	0.64	0.42	1.06	–	–	–	–	–
187.470 06	7.972 02	2.93E-15	8.97E37	–	–	–	–	–	–	187.4701	7.972 13	20.97	0.83	0.59	1.42	–	–	–	–	–
187.472 23	7.997 79	3.61E-15	1.11E38	–	–	–	–	–	–	187.472 31	7.997 85	21.98	0.53	0.3	0.83	–	–	–	–	–
187.472 34	8.007 24	3.51E-15	1.07E38	–	187.472 24	8.0072	19.08	20.54	1.47	187.472 38	8.007 41	20.03	0.86	0.56	1.42	–	–	–	–	–
187.472 29	8.0526	3.17E-15	9.71E37	–	–	–	–	–	–	187.472 38	8.052 79	22.01	0.76	0.58	1.34	–	–	–	–	–
187.476 02	8.002 71	4.86E-15	1.49E38	–	–	–	–	–	–	187.476 11	8.002 88	21.34	0.55	0.46	1.01	–	–	–	–	–
187.482 87	8.000 96	1.57E-15	4.81E37	–	–	–	–	–	–	187.482 87	8.001 12	21.89	0.92	0.57	1.49	–	–	–	–	–
187.483 01	7.956 25	2.27E-15	6.95E37	–	–	–	–	–	–	187.483 01	7.956 49	20.74	0.93	0.58	1.51	–	–	–	–	–
187.484 83	8.008 48	4.12E-15	1.26E38	–	–	–	–	–	–	187.484 89	8.008 65	21.86	0.95	0.6	1.55	–	–	–	–	–
187.490 21	7.9924	1.71E-15	5.24E37	–	–	–	–	–	–	187.490 16	7.992 68	21.44	0.61	0.51	1.12	–	–	–	–	–
187.409 46	8.003 56	1.14E-15	3.49E37	–	187.409 24	8.003 42	21.22	22.62	1.4	–	–	–	–	–	–	–	–	–	–	–
187.410 46	7.991 52	1.84E-15	5.63E37	–	187.410 33	7.991 47	21.39	22.83	1.44	–	–	–	–	–	–	–	–	–	–	–
187.413 14	7.994 75	2.74E-15	8.39E37	–	187.413 07	7.9947	21.61	23.05	1.44	–	–	–	–	–	–	–	–	–	–	–
187.415 24	7.991 26	1.67E-15	5.11E37	–	187.4151	7.991 17	21.43	22.61	1.18	–	–	–	–	–	–	–	–	–	–	–
187.415 36	7.982 63	1.33E-15	4.07E37	–	187.415 23	7.982 75	23.42	24.74	1.32	–	–	–	–	–	–	–	–	–	–	–
187.417 07	7.990 93	7.94E-15	2.43E38	–	187.416 99	7.990 86	20.44	22.06	1.62	–	–	–	–	–	–	–	–	–	–	–
187.433 43	8.020 91	1.92E-15	5.88E37	–	187.433 37	8.0209	21.12	22.78	1.66	–	–	–	–	–	–	–	–	–	–	–
187.433 75	7.978 04	6.34E-15	1.94E38	–	187.433 67	7.977 94	22.84	24.45	1.62	–	–	–	–	–	–	–	–	–	–	–
187.434 83	7.994 99	9.4E-16	2.88E37	–	187.434 71	7.994 88	21.88	23.53	1.65	–	–	–	–	–	–	–	–	–	–	–
187.437 63	7.997 41	3.48E-15	1.07E38	–	187.437 56	7.997 27	20.82	22.37	1.55	–	–	–	–	–	–	–	–	–	–	–
187.438 99	7.994 49	2.04E-15	6.25E37	–	187.438 86	7.994 42	21.95	23.6	1.65	–	–	–	–	–	–	–	–	–	–	–
187.4391	7.993 42	1.71E-15	5.24E37	–	187.439 02	7.9934	20.43	21.88	1.45	–	–	–	–	–	–	–	–	–	–	–
187.440 04	7.993 41	7.4E-16	2.27E37	–	187.44	7.993 33	22.62	24.06	1.44	–	–	–	–	–	–	–	–	–	–	–
187.440 23	7.994 62	1.04E-15	3.18E37	–	187.440 14	7.994 53	21.83	23.06	1.23	–	–	–	–	–	–	–	–	–	–	–
187.441 31	8.024 14	5.76E-15	1.76E38	–	187.4412	8.024 13	23.73	25.09	1.37	–	–	–	–	–	–	–	–	–	–	–
187.442 05	8.023 09	1.15E-15	3.52E37	–	187.442 14	8.022 92	22.12	23.53	1.41	–	–	–	–	–	–	–	–	–	–	–
187.442 31	7.989 61	3.31E-15	1.01E38	–	187.442 23	7.989 57	23.22	23.76	0.54	–	–	–	–	–	–	–	–	–	–	–
187.449 82	8.002 33	8.39E-15	2.57E38	bkg	187.449 72	8.002 22	19.41	20.82	1.41	–	–	–	–	–	–	–	–	–	–	–
187.450 34	7.994 76	1.44E-15	4.41E37	–	187.450 24	7.994 78	19.37	20.62	1.25	–	–	–	–	–	–	–	–	–	–	–
187.453 79	7.979 48	1.73E-15	5.3E37	–	187.453 86	7.979 38	21.2	22.7	1.5	–	–	–	–	–	–	–	–	–	–	–
187.456 12	7.992 93	1.86E-15	5.69E37	–	187.456 06	7.992 89	20.88	22.31	1.42	–	–	–	–	–	–	–	–	–	–	–
187.461 32	8.019 72	1.18E-15	3.61E37	–	187.461 33	8.019 67	22.69	24.33	1.65	–	–	–	–	–	–	–	–	–	–	–
187.462 25	7.987 36	1.49E-15	4.56E37	–	187.462 02	7.987 29	21.62	23.22	1.6	–	–	–	–	–	–	–	–	–	–	–
187.465 43	7.991 96	1.39E-15	4.26E37	–	187.465 22	7.9919	22.49	23.9	1.41	–	–	–	–	–	–	–	–	–	–	–
187.465 82	7.996 76	3.14E-15	9.61E37	–	187.465 84	7.996 67	22.4	23.93	1.53	–	–	–	–	–	–	–	–	–	–	–
187.469 21	8.019 33	1.96E-15	6.0E37	–	187.469 11	8.019 26	22.85	24.32	1.47	–	–	–	–	–	–	–	–	–	–	–

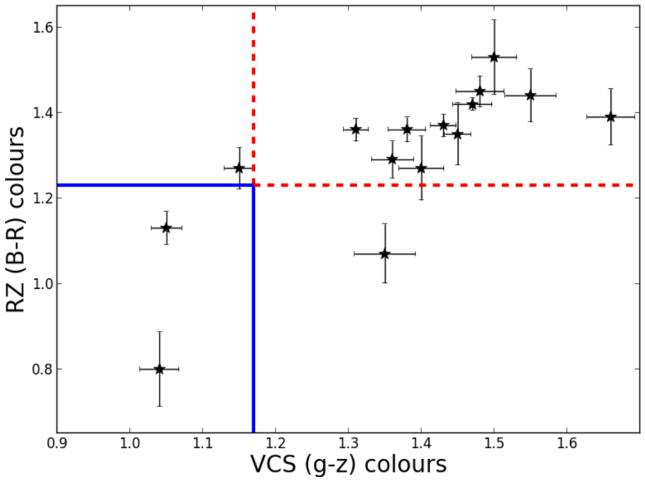

Figure 4. The VCS versus RZ colours for the clusters that appear in both catalogues. The area enclosed by the broken (solid) lines show the area of parameter space where both the VCS and the RZ classify as red (blue). The two sources for which the colours disagree are also shown.

3.2.2 Red versus blue globular cluster subpopulations

We compare the red and blue GC subpopulations to try and determine the role that GC colour, and hence metallicity, plays in LMXB formation. For some of the analysis, we combine our VCS, RZ01 and MKZ03 GC samples. This does not present a problem, even though not all GC sources have RZ01 or MKZ03 counterparts and vice versa. Colour bimodality is an intrinsic property of GC systems (Ashman & Zepf 1998). Therefore, for analysis that only requires the source to be labelled blue or red, it does not matter which photometric system was used to measure the colour of the GC. Once a GC colour has been determined and the GC has been assigned the red or blue qualitative property, we can use that to carry out further analysis. The colour bimodality of the GC system of NGC 4472 is well known and has been quantified by VCS, RZ01 and MKZ03.

For the VCS GC sample, the $g - z$ colour distribution is also bimodal, with peaks at roughly 1.1 and 1.45 and a dividing $g - z$ colour of approximately 1.17 (see fig. 6 in Jordán et al. 2009). RZ01 found that their GC sample has a bimodal $B - R$ colour distribution with peaks at 1.1 and 1.35, with a dividing $B - R$ colour of 1.23. MKZ03 found that their GCs had a dividing colour of $V - I = 1.10$, with blue and red peaks at 0.98 and 1.23, respectively. We combined the three samples and applied both X-ray and optical completeness limits, where the 100 per cent optical completeness limits are $V \sim 23.5$ (RZ01), $g = 23.3$ and $z = 22.2$ (VCS) and $V \sim 23.5$ (MKZ03). This yielded a sample of 54 GCs hosting X-ray sources. We then found two GCs for which the colour assignments did not match across the three catalogues; these two clusters were not included in the analysis. The final completeness limited sample therefore consists of 37 red and 7 blue GCs. Fig. 4 shows the VCS versus RZ colours for the clusters that appear in both catalogues. There is good agreement between the colours across the catalogues. The two sources for which there is a disagreement between the colours are also shown.

The ratio of red to blue GCs hosting X-ray sources to be 5.3±3.0. When we account for the slightly larger number of blue GCs across the three samples, we find that ratio of red to blue GCs hosting X-ray ray sources to be 5.8±2.8. Previous studies (see e.g. Kundu et al. 2002; Maccarone et al. 2003; Jordán et al. 2004; Sivakoff et al. 2007) have found that red GCs are roughly three times more likely to host a LMXB than blue GCs. Jordán et al. (2004) provide the figure with the largest error, 3±1.

The mean 0.5–5 keV luminosity for the red and blue subpopulations are 1.1±1.2 × 10^{38} erg s^{-1} and 1.3±0.4 × 10^{38} erg s^{-1}, respectively; they are statistically indistinguishable. However, using an AD test, we find the probability that the two X-ray luminosity distributions are drawn from the same sample to be only 4.9 per cent. Thus there is evidence that the red and blue GC–LMXB populations have different luminosity functions. This result is in contrast to the findings of Kim et al. (2013) and Peacock & Zepf (2016) who found that the XLFs of red and blue subpopulations were similar across a large luminosity range.

The radial distributions of the red and blue GC subpopulations were analysed. The mean radial distances for red and blue GC subpopulations were found to be 1.6±0.8 arcmin and 2.0±0.6 arcmin, respectively. Using an AD test, we find that the probability of the two distributions being drawn from the same sample is 18 per cent. Thus there is no evidence to suggest that red and blue GC subpopulations have different radial distributions.

4 CONCLUSIONS

We have found 238 X-ray point sources in the central 3.7 arcmin of NGC 4472; of which 191 were brighter than the 4 σ completeness limit of 6.3 × 10^{-16} erg s^{-1} cm^{-2} (0.5-2 keV). The completeness limited XLF is well fitted by a single PL model with slope and normalization of $2.03^{+0.16}_{-0.15}$ and $68.53^{+8.95}_{-8.28}$, respectively. Eighty of the 238 LMXBs in NGC 4472 are found to reside in GCs. We have shown that there is no significant difference between the X-ray luminosities of the LMXBs in the field and those found in GCs.

Our study also shows that within the GC–LMXB population, the X-ray sources are preferentially found in red GCs at a ratio of roughly six to one. Our analysis of the red and blue GC subpopulations shows that they have indistinguishable radial distributions. However, there is evidence to suggest that the luminosity distributions of the red and blue GC–LMXB populations differ significantly in contrast to other GC–LMXB systems.

ACKNOWLEDGEMENTS

TDJ acknowledges support from the Stobie-SALT studentship, funded jointly by the National Research Foundation of South Africa, the British Council and the University of Southampton. TDJ acknowledges the South Africa National Research Foundation Square Kilometre Array Research Fellowship. This material is based upon work supported by the National Aeronautics and Space Administration under Grants No. NAS8-03060 and GO1-12160X. This research has made use of data obtained from the Chandra Data Archive and software provided by the Chandra X-ray Center (CXC) in the application packages CIAO and CHIPS. TDJ would also like to thank Texas Tech University for its hospitality while this work was being finished and Mark Burke for his assistance.

REFERENCES

Arnaud K. A., 1996, in Jacoby G. H., Barnes J., eds, ASP Conf. Ser. Vol. 101, Astronomical Data Analysis Software and Systems V. Astron. Soc. Pac., San Francisco, p. 17
Ashman K. M., Zepf S. E., 1998, Cambridge Astrophys. Ser., 118, 387
Clark G. W., 1975, ApJ, 199, L143
Côté P., McLaughlin D. E., Cohen J. G., Blakeslee J. P., 2003, ApJ, 591, 850

Côté P. et al., 2004, ApJS, 153, 223
Fabbiano G., Blake S. et al., 2010, ApJ, 725,1805
Fabian A. C., Pringle J. E., Rees M. J., 1975, MNRAS, 172, 15P
Gilfanov M., 2004, MNRAS, 349, 146
Grimm H.-J., Gilfanov M., Sunyaev R., 2003, Chin. J. Astron. Astrophys. Suppl., 3, 257
Hills J. G., 1976, MNRAS, 175, 1P
Jordán A. et al., 2004, ApJ, 613, 279
Jordán A. et al., 2009, ApJS, 180, 54
Kim E., Kim D.-W., Fabbiano G., Lee M. G., Park H. S., Geisler D., Dirsch B., 2006, ApJ, 647, 276
Kim D.-W., Fabbiano G., 2004, ApJ, 611, 846
Kim D.-W. et al., 2006, ApJ, 652, 1090
Kim D.-W. et al., 2009, ApJ, 703, 829
Kim D.-W., Fabbiano G., Ivanova N., Fragos T. Jordán A., Sivakoff G. R., Voss R., 2013, ApJ, 764, 98
Kundu A., Whitmore B. C., 2001, AJ, 121, 2950
Kundu A., Maccarone T. J., Zepf S. E., 2002, ApJ, 574, L5
Lehmer B. D., Berkeley M., Zezas A. et al., 2014, ApJ, 789, 52
Maccarone T. J., Kundu A., Zepf S. E., 2003, ApJ, 586, 814 (MKZ03)
Maccarone T. J., Kundu A., Zepf S. E., Rhode K. L., 2010, MNRAS, 409, L84
Maccarone T. J. et al., 2016, MNRAS, 458, 3633
Macri L. M. et al., 1999, ApJ, 521, 155
Peacock M. B., Zepf S. E., 2016, ApJ, 818, 33
Rhode K. L., Zepf S. E., 2001, AJ, 121, 210 (RZ01)
Sarazin C. L., Irwin J. A., Bregman J. N., 2000, ApJ, 544, L101
Sell P. H., Pooley D., Zezas A., Heinz S., Homan J., Lewin W. H. G., 2011, ApJ, 735, 26
Sivakoff G. R. et al., 2007, ApJ, 660, 1246
Taylor M. B., 2005, in Shopbell P., Britton M., Ebert. R., eds, ASP Conf. Ser. Vol. 347, Astronomical Data Analysis Software and Systems XIV. Astron. Soc. Pac., San Francisco, p. 29
Tozzi P. et al., 2001, ApJ, 562, 42
Verbunt F., 1987, ApJ, 312, L23
Voss R., Gilfanov M., 2006, A&A, 447, 71
Voss R. et al., 2009, ApJ, 701, 471
Weisskopf M. C., Tananbaum H. D., Van Speybroeck L. P., O'Dell S. L., 2000, in Truemper J. E., Aschenbach B., eds, Proc. SPIE Conf. Ser. Vol. 4012, X-Ray Optics, Instruments, and Missions III. SPIE, Bellingham, p. 2
Zhang Z. et al., 2011, A&A, 533, A33

This paper has been typeset from a TEX/LATEX file prepared by the author.